JOURNAL OF SYNCHROTRON RADIATION

ISSN 1600-5775

Received 18 November 2015
Accepted 19 January 2016

Edited by R. W. Strange, University of Liverpool, UK

Keywords: EXAFS; molecular dynamics; reverse Monte Carlo; evolutionary algorithm; yttria.

Temperature-dependent EXAFS study of the local structure and lattice dynamics in cubic Y_2O_3

Inga Jonane,[a] Karlis Lazdins,[a] Janis Timoshenko,[a]* Alexei Kuzmin,[a] Juris Purans,[a] Pavel Vladimirov,[b] Tim Gräning[b] and Jan Hoffmann[b]

[a]Institute of Solid State Physics, University of Latvia, Kengaraga Street 8, Riga LV-1063, Latvia, and [b]Institute for Applied Materials–Applied Materials Physics, Karlsruhe Institute of Technology, Eggenstein-Leopoldshafen, PO Box 3640, 76021 Karlsruhe, Germany. *Correspondence e-mail: janis.timoshenko@gmail.com

The local structure and lattice dynamics in cubic Y_2O_3 were studied at the Y *K*-edge by X-ray absorption spectroscopy in the temperature range from 300 to 1273 K. The temperature dependence of the extended X-ray absorption fine structure was successfully interpreted using classical molecular dynamics and a novel reverse Monte Carlo method, coupled with the evolutionary algorithm. The obtained results allowed the temperature dependence of the yttria atomic structure to be followed up to ~6 Å and to validate two force-field models.

1. Introduction

Yttrium sesquioxide (yttria, Y_2O_3) is an important technological material, which is employed in pure, doped or nanosized forms. For instance, it is used as a phosphor in optical display and lighting applications (Igarashi *et al.*, 2000; Schmechel *et al.*, 2001; Capobianco *et al.*, 2002), in rare-earth ion doped lasers (Xu *et al.*, 1997; Lu *et al.*, 2001), for ethanol steam reforming in fuel-cell applications (Sun *et al.*, 2005) and in the production of ceramic materials (Wang *et al.*, 2013). During the last decade Y_2O_3 has attracted much attention since it was shown that mechanical properties and radiation resistance of steels can be improved by an addition of yttrium compounds during the manufacturing process leading to the formation of nanosized yttrium oxide within the steel matrix (Ukai & Fujiwara, 2002; Klueh *et al.*, 2002; Schneibel *et al.*, 2007). Such oxide-dispersion-strengthened (ODS) steels are considered now as promising structural materials for concentrated solar power plants and jet engines, and, in particular, for fusion and fission nuclear reactors (Lindau *et al.*, 2002).

The understanding and improving of ODS steel properties at the atomic scale represents a complicated task, whose solution requires the use of modern experimental and theoretical approaches. Among different experimental techniques, X-ray absorption spectroscopy (XAS) is able to probe the local atomic structure and lattice dynamics in bulk and nanocrystalline materials around both concentrated and diluted elements (Lee *et al.*, 1981; Aksenov *et al.*, 2006; Yano & Yachandra, 2009). Therefore its application to the case of ODS steels was naturally started during the last ten years (Degueldre *et al.*, 2005; Pouchon *et al.*, 2007; Béchade *et al.*, 2012; He *et al.*, 2012; Liu *et al.*, 2014; Menut *et al.*, 2015; Cintins *et al.*, 2015). On the other hand, one expects that large-scale molecular dynamics (MD) (Hirata *et al.*, 2011; Yashiro *et al.*, 2012) and Monte Carlo (Alinger *et al.*, 2007; Hin *et al.*, 2009) simulations will contribute to the interpretation and predic-

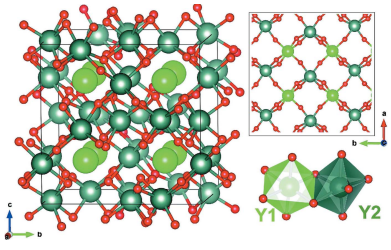

tion of experimental results. The reliability of these theoretical models is directly related to how well the interatomic interactions can be described in the steel matrix, within the oxide nanoparticles and between the nanoparticles and the matrix. This question can be addressed using the MD-EXAFS method (Kuzmin & Evarestov, 2009), which allows validation of interatomic potentials by direct comparison of experimentally measured extended X-ray absorption fine structure (EXAFS) with theoretically simulated ones. However, the accurate simulation of yttrium oxide nanoparticles, embedded in a steel matrix, or even of free-standing yttria particles is truly challenging, and therefore we have started from their bulk ancestor. Note also that for practical applications (*e.g.* for modelling of ODS materials) it is important to demonstrate that the chosen interatomic potentials are reliable over a broad temperature range and are able to reproduce the evolution of material local structure upon temperature increase. Therefore, in this study, we used EXAFS data acquired in the temperature range from 300 to 1273 K.

Cubic yttrium sesquioxide (c-Y_2O_3), known also as α-Y_2O_3, has complex crystallographic structure and belongs to the space group $Ia\bar{3}$ with $Z = 16$ (Fig. 1). Its lattice parameter is equal to $a_0 = 10.604$ Å at $T = 300$ K (Bonnet *et al.*, 1975) [the range of values reported in the literature is 10.6021–10.6042 Å (Carlson, 1990)]. There are two non-equivalent yttrium atoms Y1 and Y2 located at the Wyckoff positions 8*b*(0.25, 0.25, 0.25) and 24*d*(*u*, 0, 0.25) [$u = -0.0326$ at $T = 300$ K (Bonnet *et al.*, 1975)], respectively, and the oxygen atoms occupy 48*c*(*x*, *y*, *z*) positions [$x = 0.3911$, $y = 0.1519$, $z = 0.3806$ at $T = 300$ K (Bonnet *et al.*, 1975)]. As a result, Y1 atoms have regular octahedral coordination with six equivalent bond lengths R(Y1—O) = 2.89 Å, whereas Y2 atoms are located in distorted octahedral environment with three groups of slightly different distances R(Y2—O) = 2 × 2.24 Å, 2 × 2.27 Å and 2 × 2.33 Å.

The structural parameters do not change significantly below room temperature down to 77 K (Faucher & Pannetier, 1980). However, the lattice parameter of c-Y_2O_3 increases non-linearly up to 2512 ± 25 K, where a phase transition into the fluorite-type structure (space group $Fm\bar{3}$) occurs, followed by melting at 2705 ± 25 K (Swamy *et al.*, 1999).

The lattice dynamics of c-Y_2O_3 have been studied experimentally and theoretically. Bose *et al.* (2011) performed neutron inelastic scattering measurements of the phonon density of states and lattice dynamic calculations using first-principles density functional theory and force-field interatomic potential model.

Classical MD simulations of c-Y_2O_3 were reported in several papers (Bose *et al.*, 2011; Álvarez *et al.*, 1999; Belonoshko *et al.*, 2001; Lau & Dunlap, 2011), and the results obtained in the two most recent studies (Bose *et al.*, 2011; Lau & Dunlap, 2011) will be considered further.

In this study we employed two advanced methods: (i) MD-EXAFS (Kuzmin & Evarestov, 2009) and (ii) the novel reverse Monte Carlo/evolutionary algorithm approach (RMC/EA-EXAFS) (Timoshenko *et al.*, 2014*a*) for the interpretation of temperature-dependent Y *K*-edge EXAFS in c-Y_2O_3. First, we used the MD-EXAFS method (Kuzmin & Evarestov, 2009) to validate the quality of the most recent force-field models based on pair potentials (Bose *et al.*, 2011; Lau & Dunlap, 2011). Next, to analyze the validity of the chosen force-field models quantitatively, we compared the three-dimensional structure models, obtained in the MD calculations, with those constructed directly from the experimental EXAFS data *via* the RMC/EA-EXAFS approach (Timoshenko *et al.*, 2012, 2014*a*). Such combined approach allows one to analyze in detail the nearest-neighbour interactions, and to follow their evolution upon temperature increase.

Note that both MD-EXAFS and RMC/EA-EXAFS approaches were successfully employed by us recently to a number of crystalline materials such as $SrTiO_3$ (Kuzmin & Evarestov, 2009), ReO_3 (Timoshenko *et al.*, 2012, 2013, 2014*a*; Kalinko *et al.*, 2009), $LaCoO_3$ (Kuzmin *et al.*, 2011), Ge (Timoshenko *et al.*, 2011, 2012), NiO (Anspoks *et al.*, 2012), H_xReO_3 (Timoshenko *et al.*, 2014*a*), ZnO (Timoshenko *et al.*, 2014*b*,*c*) and various tungstates (Kalinko & Kuzmin, 2013; Timoshenko *et al.*, 2014*d*, 2015).

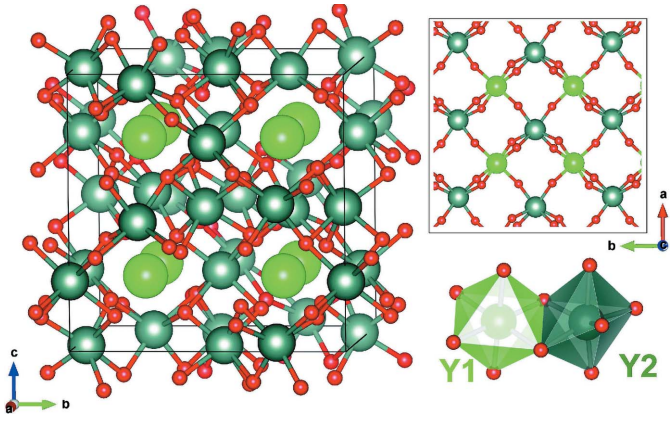

Figure 1
Crystal structure of cubic Y_2O_3 (Bonnet *et al.*, 1975; Faucher & Pannetier, 1980). The regular and distorted octahedra around non-equivalent yttrium atoms (Y1 and Y2) are also shown.

2. Experimental and data analysis

X-ray absorption spectra of cubic Y_2O_3 (99.99%, Sigma-Aldrich) were recorded at the Y *K*-edge (17038 eV) in transmission mode at the ELETTRA (Trieste, Italy) XAFS bending-magnet beamline (Di Cicco *et al.*, 2009). The storage ring operated in the top-up multibunch mode at the energy $E = 2$ GeV and current $I = 310$ mA. The synchrotron radiation was monochromated using a Si(111) double-crystal monochromator, and its intensity before and after the sample was measured by two ionization chambers. Yttrium metallic foil (99%, GoodFellow) was used for energy calibration. Polycrystalline c-Y_2O_3 powder was mixed with boron nitride and pressed into pellets. The sample thickness was optimized to obtain the absorption Y *K*-edge jump value $\Delta\mu \simeq 1$. The sample temperature was controlled using the l'Aquila-Camerino glass furnace (Di Cicco *et al.*, 2009) for high-temperature measurements in the range from 300 to 1273 K.

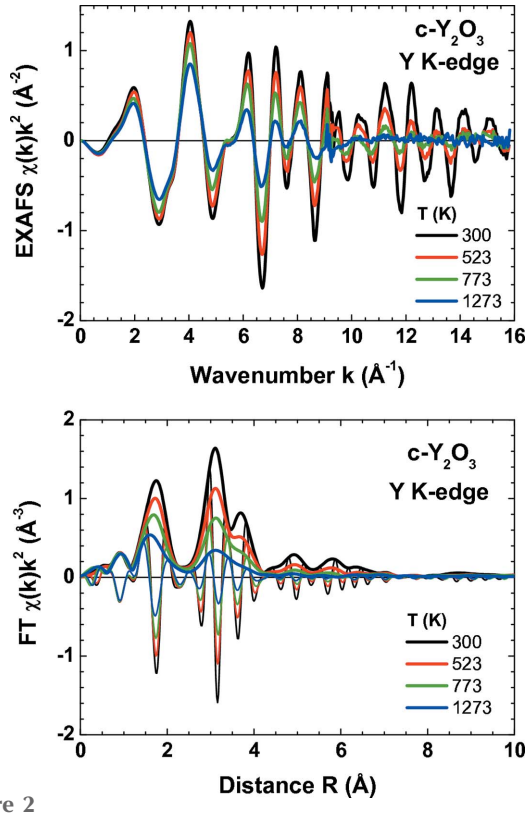

Figure 2
Temperature-dependence of the experimental Y *K*-edge EXAFS spectra $\chi(k)k^2$ and their (phase-uncorrected) Fourier transforms (FTs) for c-Y_2O_3 at several selected temperatures. Both the magnitude and imaginary parts of the FTs are shown.

The experimental Y *K*-edge EXAFS spectra were extracted using the conventional procedure (Aksenov *et al.*, 2006; Kuzmin, 1995) and are shown together with their Fourier transforms (FTs) in Fig. 2. The position of the photoelectron energy origin E_0 was set at 17050 eV to be in agreement with the theoretical one obtained by the *FEFF8* code (Ankudinov *et al.*, 1998). The first peak in the FT at ∼1.7 Å is due to the contribution of the first coordination shell (six closest oxygen atoms) around the absorbing yttrium atom, whereas the second peak, at 3.5 Å, having a double-peak shape at room temperature, originates mainly due to the second and third coordination shells formed by yttrium atoms. Note that six Y atoms in the second coordination shell are located at about 3.5 Å from the absorbing yttrium atom, and their YO_6 octahedra share a common edge with that of the absorbing yttrium; the distance between six Y atoms in the third coordination shell and the absorbing yttrium atom is about 4.0 Å, and their YO_6 octahedra are connected through a common vertex (Fig. 1).

3. Molecular dynamics simulations

Classical molecular dynamics simulations were performed using the *GULP* code (Gale, 1996; Gale & Rohl, 2003) in the canonical (NVT) ensemble with periodic boundary conditions. The simulation box had a size of a $2a_0 \times 2a_0 \times 2a_0$ supercell including 640 atoms. The starting configuration was set to the mean crystallographic c-Y_2O_3 structure (Bonnet *et al.*, 1975). A Nosé–Hoover thermostat (Hoover, 1985) was used to maintain the required average temperature during each simulation. Newton's equations of motion were integrated using the Verlet leapfrog algorithm (Hockney, 1970) with a time step of 0.5 fs. The equilibration and production times were 20 ps each. The simulations were performed at temperatures in the range from 297 K to 1273 K, corresponding to that of the EXAFS experiments. A set of 4000 atomic configurations were accumulated during each production run, and the Y *K*-edge EXAFS spectra were calculated for two non-equivalent yttrium atoms (Y1 and Y2) in each MD configuration using the *ab initio* real-space multiple-scattering *FEFF8* code (Ankudinov *et al.*, 1998; Rehr & Albers, 2000). Finally, the configuration-averaged Y *K*-edge EXAFS spectra were obtained (Kuzmin & Evarestov, 2009) and used for direct comparison with the experimental ones.

Table 1
Buckingham potential parameters for the Y—O and O—O atom pairs used in molecular dynamics simulations.

	A (eV)	ρ (Å)	C (eV Å^6)
Model 1 (Bose *et al.*, 2011)			
Y—O	1822	0.309042	0.0
O—O	1822	0.305726	100.0
Model 2 (Lau & Dunlop, 2011)			
Y—O	1642.724	0.353197	104.180
O—O	2056.49	0.361402	271.761

The multiple-scattering contributions were accounted up to the seventh order. Note, however, that the influence of such contributions for investigated material is quite small. The calculation of the cluster potential was performed only once for the mean crystallographic c-Y_2O_3 structure (Bonnet *et al.*, 1975), thus neglecting its small variation due to thermal disorder. The complex exchange-correlation Hedin–Lundqvist potential and default values of muffin-tin radii [R_{mt}(Y) = 1.57 Å and R_{mt}(O) = 1.06 Å], as provided within the *FEFF8* code (Ankudinov *et al.*, 1998), were employed.

Two force-field models (Bose *et al.*, 2011; Lau & Dunlap, 2011), based on the rigid-ion Buckingham potential, were used in the MD simulations to describe interactions in c-Y_2O_3 (Table 1),

$$U_{ij}(r_{ij}) = A_{ij}\exp\left(-\frac{r_{ij}}{\rho_{ij}}\right) - \frac{C_{ij}}{r_{ij}^6} + \frac{q_i q_j e^2}{r_{ij}}. \qquad (1)$$

The Coulomb interactions were described using the effective ion charges q(Y) = +2.4 and q(O) = −1.6 in the first model (Model 1) (Bose *et al.*, 2011), whereas the formal ion charges [q(Y) = +3 and q(O) = −2] were assumed in the second model (Model 2) (Lau & Dunlap, 2011).

Several properties of c-Y_2O_3 such as the lattice parameter, bulk modulus (B_0) and elastic constants (C_{11}, C_{12} and C_{44}) were calculated using two force-field models (Bose *et al.*, 2011; Lau & Dunlap, 2011) and are compared with the available experimental data (Faucher & Pannetier, 1980; Palko *et al.*,

Table 2
Experimental (Faucher & Pannetier, 1980; Palko *et al.*, 2001) and calculated properties of c-Y_2O_3.

	Experiment	Model 1 (Bose *et al.*, 2011)	Model 2 (Lau & Dunlop, 2011)
Lattice parameter (Å)	10.6073	10.58	10.61
Bulk modulus B_0 (GPa)	156	137	182
Elastic constant C_{11} (GPa)	223.7	204	292
Elastic constant C_{12} (GPa)	112.4	103	127
Elastic constant C_{44} (GPa)	74.6	79	85

2001) in Table 2. As one can see, both models reproduce the experimental values equally well.

The experimental Y *K*-edge EXAFS and configuration-averaged MD-EXAFS spectra, calculated using two models, and their Fourier transforms are compared in Fig. 3 for the two extreme temperatures (300 and 1273 K). The first model (Model 1) gives an overall good agreement with experimental data, except for some small discrepancy in the FT peaks amplitude at 300 K due to the underestimation of the YO_6 octahedra distortion in the model. The second model (Model 2) fails significantly at 300 K in the description of peaks located between 1 and 4 Å in the FT, and the discrepancy remains for the first shell at 1273 K. In fact, the difference at 300 K for Model 2 is also well observed in *k*-space.

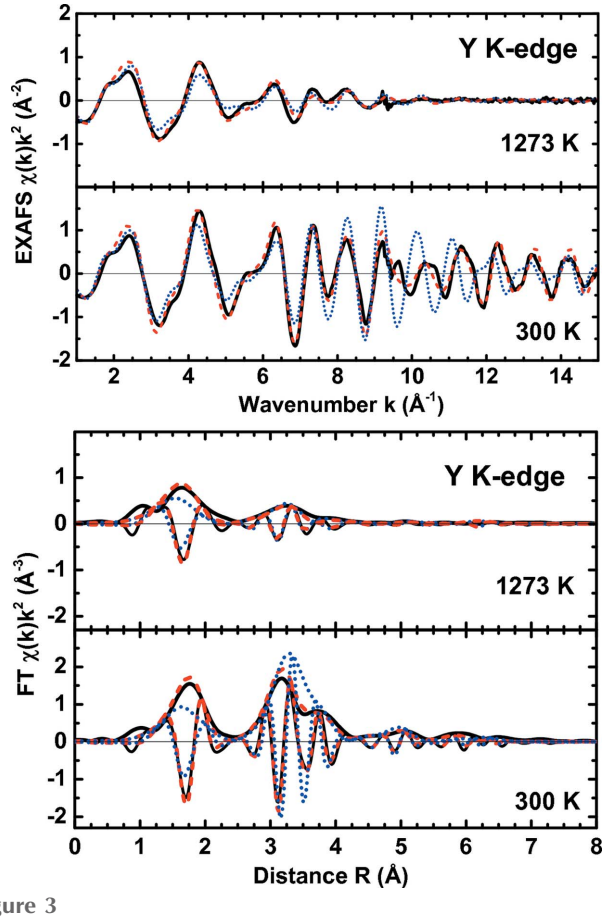

Figure 3
Comparison between the experimental (solid lines) and MD-EXAFS calculated [dashed lines: Model 1 (Bose *et al.*, 2011); dotted lines: Model 2 (Lau & Dunlap, 2011)] Y *K*-edge EXAFS spectra $\chi(k)k^2$ and their (phase-uncorrected) Fourier transforms for c-Y_2O_3 at 300 and 1273 K. Both the magnitude and imaginary parts of the FTs are shown.

To analyze the validity of Model 1 in more detail and to validate the temperature-dependencies of interactions within different nearest-neighbour pairs separately, we compared the three-dimensional structure model, obtained in the MD simulations, with that constructed directly from the experimental Y *K*-edge EXAFS data using the reverse Monte Carlo approach.

4. Reverse Monte Carlo simulations

The reverse Monte Carlo (RMC) method (McGreevy & Pusztai, 1988; Timoshenko *et al.*, 2012) allows one to construct a structure model of the material based on the available experimental data (EXAFS in our case) only and does not require knowledge of interatomic potentials, which is a crucial point in MD simulations. Additionally, the RMC method can be applied to study the materials also at cryogenic temperatures, where the classical MD approach fails due to the neglect of quantum effects. On the other hand, the extraction of dynamical information (interatomic forces, frequencies of atomic oscillations) from the results of the RMC process is not straightforward. Therefore, both approaches, MD and RMC, complement each other.

Recently we have proposed an enhanced RMC approach for the analysis of EXAFS data from crystalline materials, based on the use of the evolutionary algorithm (EA). The combined RMC/EA scheme allows us to perform accurate analysis of EXAFS data from distant coordination shells, taking into account static and thermal disorder as well as multiple-scattering effects, and can be applied even for complex materials with low symmetry (Timoshenko *et al.*, 2014*a*,*d*). As in the conventional RMC method, the three-dimensional structure model of a material is optimized in the RMC/EA scheme *via* the consequent proposal of random changes of atomic coordinates, and the agreement between the experimental and configuration-averaged EXAFS spectra, calculated for the proposed structure model, is used as the only criterium for the acceptance or rejection of the proposed move. This configuration-averaged EXAFS spectrum is obtained from *ab initio* multiple-scattering calculations performed using the *FEFF8* code (Ankudinov *et al.*, 1998). Implementation of the evolutionary algorithm in the conventional RMC scheme significantly improves the convergence of the simulations: in this case we use not just one but several (32 in this study) structure models of the material simultaneously. The information exchange between the simulated structure models allows us to find the solution (*i.e.* the average atomic configuration that gives the best possible description of experimental data) much faster (Timoshenko *et al.*, 2014*a*).

Since we are interested in simulating the effect of thermal disorder in crystalline Y_2O_3, the random displacements of atoms at each RMC iteration were constrained to be smaller than 0.4 Å around their equilibrium positions, known from

diffraction experiments (Bonnet *et al.*, 1975; Faucher & Pannetier, 1980). As a result, the average atomic structure provided by our RMC simulations corresponds to the crystallographic one and the positions of atoms are distributed around the Wyckoff ones. This allowed us to follow thermal disorder effects separately around both inequivalent Y1 and Y2 atoms.

As in our MD simulations, the model of crystalline yttria in RMC/EA-EXAFS analysis is constructed as an infinite crystal employing periodic boundary conditions for the supercell composed of $2a_0 \times 2a_0 \times 2a_0$ unit cells of cubic Y_2O_3. The value of the lattice parameter a_0 = 10.607 Å was fixed at the experimental value for crystalline yttria obtained from a neutron powder diffraction experiment (Faucher & Pannetier, 1980). The Y *K*-edge EXAFS spectra were calculated for both non-equivalent yttrium positions (Y1 and Y2) separately, and then added together with weights of 1/4 and 3/4, which correspond to the ratio of Y1 and Y2 atoms in cubic Y_2O_3 structure, to obtain the total configuration-averaged EXAFS spectrum. The latter was used for the comparison with the experimental EXAFS data. The EXAFS calculations were performed using the same scattering paths and cluster potential as for the MD simulations. The experimental and calculated Y *K*-edge EXAFS spectra at each iteration were compared using the Morlet wavelet transform (WT) (Muñoz *et al.*, 2003; Funke *et al.*, 2005; Timoshenko & Kuzmin, 2009) in the *k*-space range from 3.5 to 14.5 $Å^{-1}$ and in the *R*-space range from 1.0 to 6.9 Å. This allowed us to account for the features of EXAFS spectra in *k* and *R* spaces simultaneously.

At each temperature a good agreement between the experimental and calculated Y *K*-edge EXAFS spectra (Figs. 4 and 5) was achieved after several thousands of RMC/EA iterations. As one can see, RMC/EA modelling, unlike the MD approach, allowed us to obtain a very good description of all features of EXAFS in *k* and *R* spaces at all temperatures. The final atomic configurations then were used to estimate the structure parameters of interest, and to compare them with those obtained in our MD simulations. The final set of atomic coordinates was also used to evaluate the importance of a contribution from the multiple-scattering (MS) effects to the total EXAFS spectrum (Fig. 4). As one can see, the MS contribution in cubic Y_2O_3 is quite small but not negligible over the whole *k*-range. Moreover, an account of the MS effects is important to correctly describe the FT peaks at ~3.7 Å and 6 Å: here the main MS contributions come from the octahedral environment around the absorbing yttrium atoms in the first (oxygen) and second (yttrium) coordination shells, respectively.

5. Discussion

To compare the structure models, obtained by MD and RMC/EA simulations, one can calculate the atomic radial distribution functions (RDFs) around both Y1 and Y2 (Fig. 6). Note that, while the distribution of atoms in the outer coordination shells of Y1 and Y2 differs significantly, the first three peaks of RDFs have close shapes and positions for both non-equivalent

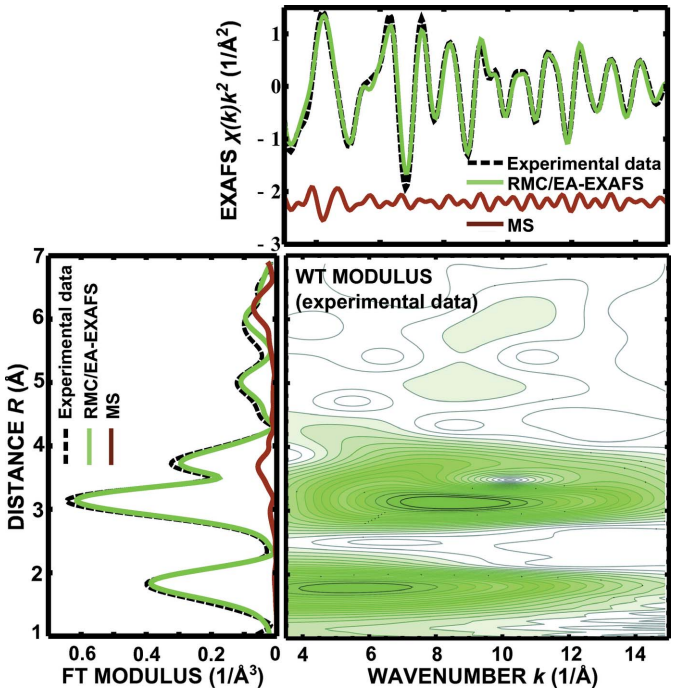

Figure 4
Results of RMC/EA-EXAFS calculations for c-Y_2O_3 at room temperature: comparison of experimental and calculated (RMC/EA) Y *K*-edge EXAFS spectra $\chi(k)k^2$ (upper panel) and their Fourier transforms (bottom left panel), and the Morlet wavelet image of the experimental Y *K*-edge EXAFS spectrum (bottom right panel). The multiple-scattering (MS) contribution to the total EXAFS spectrum is also shown.

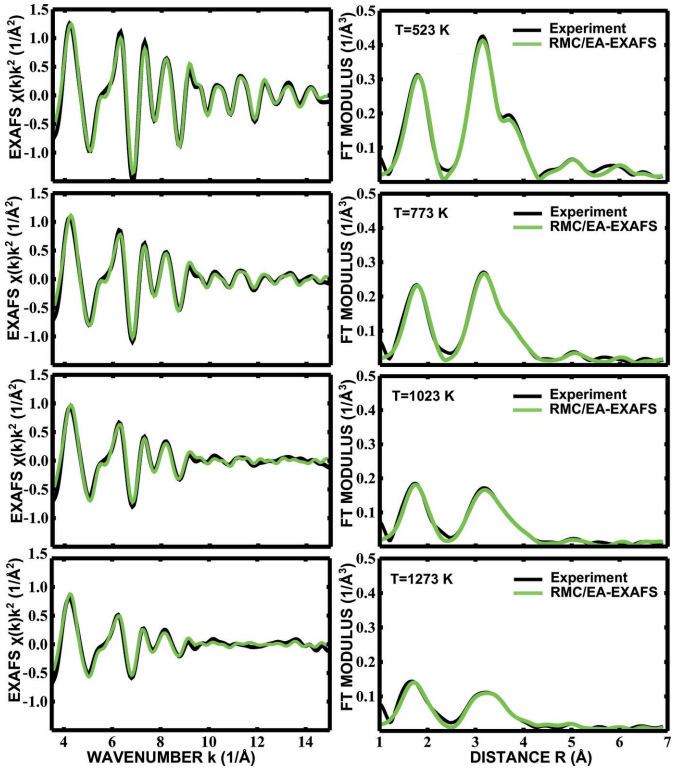

Figure 5
Results of RMC/EA-EXAFS calculations for c-Y_2O_3 at temperatures from 523 up to 1273 K: comparison of the experimental and calculated (RMC/EA) Y *K*-edge EXAFS spectra $\chi(k)k^2$ (left panels) and their Fourier transforms (right panels).

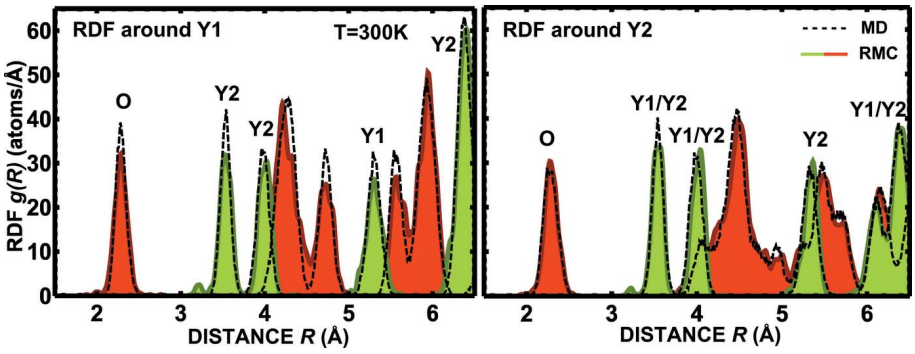

Figure 6
RDFs around non-equivalent Y1 and Y2 sites, obtained in RMC/EA and MD (Model 1) simulations for T = 300 K.

yttrium sites. We will limit our further discussion to these peaks only.

Comparison of RDFs for Y—O and Y—Y atom pairs at room temperature indicates that both RMC/EA and MD methods give close results. However, one can note that the width of the peaks in the RDF around Y1 is systematically narrower and, hence, the peaks are higher in the case of the MD results.

To make the comparison more quantitative and to follow temperature-dependent variations, we have extracted the mean square relative displacement (MSRD) factors, containing contributions from both static and thermal disorder, from the widths of RDF peaks: their temperature-dependencies for the first three coordination shells are shown in Fig. 7. The uncertainties of the RMC/EA results were estimated by repeating calculations several times with different sequences of pseudo-random numbers (Timoshenko *et al.*, 2014*a*). Temperature-dependencies of the MSRDs, obtained from RMC/EA results, were best fitted using the correlated Einstein model (Sevillano *et al.*, 1979) (solid lines in Fig. 7). Using the obtained value of the Einstein frequency ω_E, one can estimate the effective bond-strength constant $\kappa = \omega_E^2\mu$, where μ is the reduced mass of the atomic pair. For the MD results, in turn, the corresponding effective bond-strength constants can be calculated simply from the slopes of the temperature-dependencies of the MSRD factors, since MSRD(T) = k_BT/κ (T is the absolute temperature and k_B is the Boltzmann's constant). Hence the obtained temperature dependencies of the MSRD factors can be used to validate the strength of interatomic interactions in the MD model. The values of κ obtained in the MD and RMC/EA simulations are compared in Table 3.

Note that our RMC/EA results suggest that the corresponding MSRD factors for the nearest neighbours of non-equivalent Y1 and Y2 atoms are close. For RMC/EA results we cannot discriminate between non-equivalent Y2—O bonds in the first coordination shell within the uncertainties of the analysis. We also do not observe any significant difference in the MSRD values for Y1—O and Y2—O pairs. Similarly, we do not detect any significant differences in the MSRD values for Y1—Y2 and Y2—Y2 pairs in the third coordination shell. For the Y—Y pairs in the second coordination shell, in turn, only minor difference in the static disorder contribution was observed.

From the results, summarized in Figs. 7(*b*)–7(*d*) and in Table 3, one can see that MSRD factors, obtained in the MD simulations and extracted from experimental EXAFS data using RMC/EA methods, are close at room temperature, and the temperature-dependencies of MSRD factors for all three coordination shells of yttrium are also close. The estimated effective bond-strength constant values for the first coordination shell, obtained by MD and RMC/EA methods, agree well and are also close to that determined by infra-red and Raman spectroscopies [103 N m^{-1} (Repelin *et al.*, 1995) and 108 N m^{-1} (Ubaldini & Carnasciali, 2008)]. Thus one can

Table 3
Effective bond-strength constants κ_1, κ_2 and κ_3 for the first (Y1—O), second (Y1—Y2) and third (Y1—Y2) coordination shells of Y1 atoms, respectively, obtained from the results of MD (Model 1; Bose *et al.*, 2011) and RMC/EA simulations for c-Y_2O_3 in the temperature range from 300 to 1273 K.

Effective bond-strength constant (N m^{-1})	MD	RMC/EA
κ_1	88.8	101 ± 5
κ_2	103.9	116 ± 7
κ_3	79.0	107 ± 9

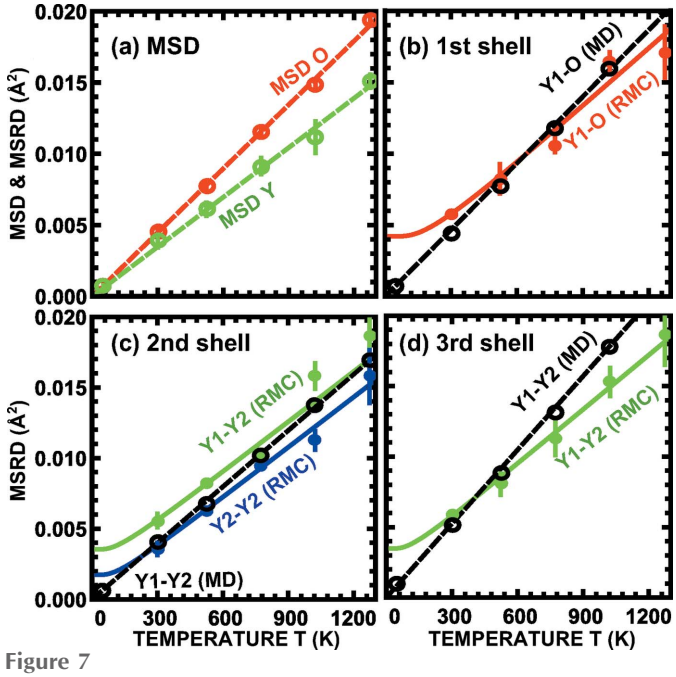

Figure 7
Calculated MSD (*a*) and MSRD factors for the first (Y—O) coordination shell (*b*), for the second (Y—Y) coordination shell (*c*) and for the third (Y—Y) coordination shell (*d*). MSD and MSRD values obtained from the MD simulations for Model 1 are shown by dashed straight lines and open circles. MSRD values obtained by the RMC/EA method are shown by filled circles, while solid lines correspond to their fit by the Einstein model.

conclude that the pairwise Y—O interactions are described with good accuracy in the used force field-model (Model 1).

Similar conclusions can be drawn for the second and third coordination shells (Y—Y pairs), Figs. 7(*c*) and 7(*d*): results obtained by RMC/EA and MD methods are in reasonable agreement. In both cases the effective bond-strength constant for the third coordination shell is smaller by about 10–20% than that for the second coordination shell. Note that from the relatively large value of κ for the first coordination shell (Y—O pairs) one may conclude that YO_6 octahedra are relatively rigid. Therefore the observed difference in the bond strengths for the Y—Y pairs in the second and third coordination shells may be attributed to their different connectivity to the absorbing yttrium atom: yttrium atoms in the second coordination shell are connected through two oxygen atoms of a common YO_6 octahedra edge, whereas yttrium atoms in the third coordination shell are connected through a common YO_6 octahedra vertex (Fig. 1).

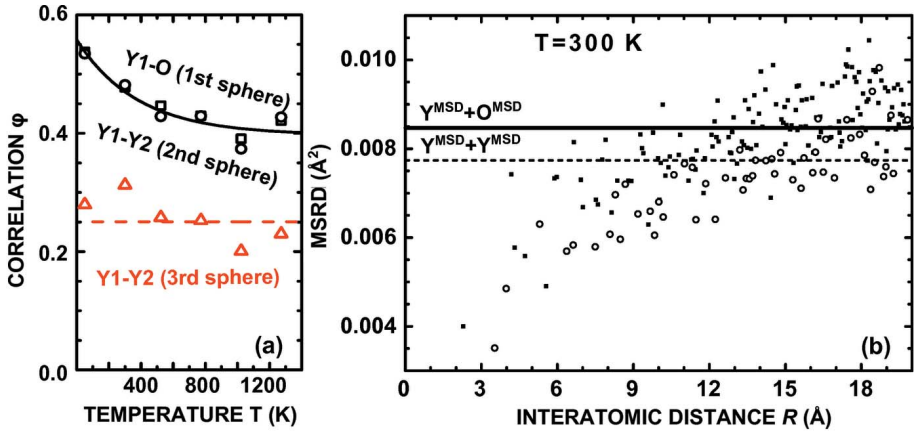

Figure 8
(*a*) Temperature-dependence of the dimensionless correlation parameter φ for the nearest Y—O (circles) and Y—Y bonds (squares and triangles). Solid and dashed lines are guides for the eye. (*b*) Calculated MSRD factors for Y—O (solid squares) and Y—Y (open circles) plotted *versus* the interatomic distance *R*. The solid line is a sum of MSDs for Y and O, the dashed line is a sum of two MSDs of Y. All results are obtained from the MD simulations at 300 K using the force-field model (Model 1) from Bose *et al.* (2011).

The obtained results suggest that the first force-field model (Model 1) is consistent with our experimental data. Therefore we can employ the results obtained in the MD simulation for detailed analysis of atomic displacements in Y_2O_3. The temperature-dependencies of isotropic mean-square displacement (MSD) factors for the Y and O atoms are shown in Fig. 7(*a*). The MSD and MSRD values for the *i*–*j* atom pair are related as $\mathrm{MSRD}_{ij} = \mathrm{MSD}_i + \mathrm{MSD}_j - 2\sqrt{\mathrm{MSD}_i}\sqrt{\mathrm{MSD}_j}\,\varphi$, where φ is a dimensionless correlation parameter (Booth *et al.*, 1995), which is equal to +1 for perfectly in-phase atom motion, to 0 for completely independent motion, and to −1 for perfectly antiphase motion. For materials without phase transitions one can expect that the value of φ depends on temperature in the low-temperature region, but reaches some saturation value at high temperatures. Using the results of our MD simulations for Model 1, we have found (Fig. 8) that the correlation parameter is $\varphi = 0.55$ at 50 K and decreases to $\varphi = 0.40$ at 1273 K for both first (Y1—O pairs) and second (Y1—Y2 pairs) coordination shells, indicating prevalent in-phase motion of nearest neighbours in c-Y_2O_3. In the third (Y1—Y2 pairs) coordination shell the correlation $\varphi \simeq 0.25$ is small and remains constant at all temperatures within the simulation error.

The variation of MSRDs for nearest Y—O and Y—Y as a function of the interatomic distance was calculated at T = 300 K from a set of atomic coordinates obtained in the MD simulations for Model 1 and is shown in Fig. 8. The values of MSRD increase and reach the sum of the MSD values for distant shells at about 9–15 Å. Only in these distant shells can the motion of atoms be considered as uncorrelated with respect to the motion of the central atom, and, hence, the corresponding MSRD values can be used directly to find the MSD values. This finding indicates that the extraction of the MSD values from EXAFS data only (using, for instance, the RMC/EA method) for crystalline yttria is, in principle, possible, but is challenging since it requires having high-quality experimental data as well as performing the analysis of distant coordination shells (Sapelkin & Bayliss, 2002; Jeong *et al.*, 2003).

6. Conclusions

Local atomic structure and lattice dynamics in cubic Y_2O_3 were studied in the temperature range from 300 to 1273 K by X-ray absorption spectroscopy. The experimental Y *K*-edge EXAFS data were analysed by reverse Monte Carlo/evolutionary algorithm simulations and were also used to validate by the MD-EXAFS method (Kuzmin & Evarestov, 2009) two force-field models (Bose *et al.*, 2011; Lau & Dunlap, 2011), which were employed in the classical molecular dynamics simulations and are based on the Buckingham potential. We found that, while both force-field models give close values of the lattice parameter, bulk modulus (B_0) and elastic constants (C_{11}, C_{12} and C_{44}) (Table 2) in rather good agreement with the available experimental data (Faucher & Pannetier, 1980; Palko *et al.*, 2001), the second force-field model (Model 2) from Lau & Dunlap (2011) fails to reproduce the temperature-dependence of the EXAFS spectra. Thus the EXAFS spectra provide additional information on the structure and dynamics of bulk cubic Y_2O_3, which allows one to discriminate such close theoretical models as shown by Bose *et al.* (2011) and Lau & Dunlap (2011).

The MD simulations performed using the force-field model (Model 1) from Bose *et al.* (2011) give configuration-averaged EXAFS spectra in rather good agreement with the experimental data at all temperatures, except for a small discrepancy in the broadening of the first and second coordination shells

at 300 K. This discrepancy is due to the pair-potential model, which is not able to account properly for YO_6 octahedra distortions in cubic Y_2O_3. Further, we compared the structure model, obtained in the MD simulations, with the one constructed directly from the experimental data using the RMC/EA approach and found that temperature-dependencies of the pair-wise interactions at least for the first three coordination shells are reproduced rather well with the force-field model (Model 1) developed by Bose *et al.* (2011).

We found that the difference in the local dynamics around non-equivalent Y1 and Y2 sites is not large. At the same time, our analysis suggests that there are significant differences in the temperature effect on the interaction of Y—Y pairs in the second and third coordination shells, despite the fact that corresponding interatomic distances are close.

The results of the MD simulations also suggest a decrease of the correlation in atomic motion with increasing temperature for nearest atom pairs in the first and second coordination shells, whereas the correlation effects are smaller and remain constant in the third coordination shell. We also found from the MD simulations that the correlation in atomic motion decreases in distant coordination shells (above 9 Å), providing the possibility to estimate the values of MSD factors from EXAFS data directly, if accurate analysis of outer shell contributions would be possible.

Acknowledgements

This work has been carried out within the framework of the EUROfusion consortium and has received funding from the Euratom research and training programme 2014–2018 under grant agreement No 633053. The views and opinions expressed herein do not necessarily reflect those of the European Commission. We gratefully acknowledge the assistance of the XAFS beamline staff members during the EXAFS experiment. The research leading to these results has received funding from the European Community's Seventh Framework Programme (FP7/2007–2013) under Grant agreement No. 312284.

References

Aksenov, V., Koval'chuk, M. V., Kuz'min, A. Y., Purans, Y. & Tyutyunnikov, S. (2006). *Crystallogr. Rep.* **51**, 908–935.
Alinger, M., Wirth, B., Lee, H.-J. & Odette, G. (2007). *J. Nucl. Mater.* **367–370**, 153.
Álvarez, L. J., San Miguel, M. A. & Odriozola, J. A. (1999). *Phys. Rev. B*, **59**, 11303–11307.
Ankudinov, A. L., Ravel, B., Rehr, J. J. & Conradson, S. D. (1998). *Phys. Rev. B*, **58**, 7565–7576.
Anspoks, A., Kalinko, A., Kalendarev, R. & Kuzmin, A. (2012). *Phys. Rev. B*, **86**, 174114.
Béchade, J.-L., Menut, D., Lescoat, M.-L., Sitaud, B., Schlutig, S., Solari, P., Llorens, I., Hermange, H., de Carlan, Y., Ribis, J. & Toualbi, L. (2012). *J. Nucl. Mater.* **428**, 183–191.
Belonoshko, A. B., Gutierrez, G., Ahuja, R. & Johansson, B. (2001). *Phys. Rev. B*, **64**, 184103.
Bonnet, M., Delapalme, A. & Fuess, H. (1975). *Acta Cryst.* A**31**, 264–265.
Booth, C. H., Bridges, F., Bauer, E. D., Li, G. G., Boyce, J. B., Claeson, T., Chu, C. W. & Xiong, Q. (1995). *Phys. Rev. B*, **52**, R15745–R15748.
Bose, P. P., Gupta, M. K., Mittal, R., Rols, S., Achary, S. N., Tyagi, A. K. & Chaplot, S. L. (2011). *Phys. Rev. B*, **84**, 094301.
Capobianco, J. A., Vetrone, F., Boyer, J. C., Speghini, A. & Bettinelli, M. (2002). *J. Phys. Chem. B*, **106**, 1181–1187.
Carlson, O. (1990). *Bull. Alloy Phase Diagrams*, **11**, 61.
Cicco, A. D., Aquilanti, G., Minicucci, M., Principi, E., Novello, N., Cognigni, A. & Olivi, L. (2009). *J. Phys. Conf. Ser.* **190**, 012043.
Cintins, A., Anspoks, A., Purans, J., Kuzmin, A., Timoshenko, J., Vladimirov, P., Gräning, T. & Hoffmann, J. (2015). *IOP Conf. Ser. Mater. Sci. Eng.* **77**, 012029.
Degueldre, C., Conradson, S. & Hoffelner, W. (2005). *Comput. Mater. Sci.* **33**, 3–12.
Faucher, M. & Pannetier, J. (1980). *Acta Cryst.* B**36**, 3209–3211.
Funke, H., Scheinost, A. C. & Chukalina, M. (2005). *Phys. Rev. B*, **71**, 094110.
Gale, J. D. (1996). *Philos. Mag. B*, **73**, 3–19.
Gale, J. D. & Rohl, A. L. (2003). *Mol. Simul.* **29**, 291–341.
He, P., Liu, T., Möslang, A., Lindau, R., Ziegler, R., Hoffmann, J., Kurinskiy, P., Commin, L., Vladimirov, P., Nikitenko, S. & Silveir, M. (2012). *Mater. Chem. Phys.* **136**, 990–998.
Hin, C., Wirth, B. D. & Neaton, J. B. (2009). *Phys. Rev. B*, **80**, 134118.
Hirata, A., Fujita, T., Wen, Y. R., Schneibel, J. H., Liu, C. T. & Chen, M. W. (2011). *Nat. Mater.* **10**, 922–926.
Hockney, R. W. (1970). *Methods Comput. Phys.* **9**, 136.
Hoover, W. G. (1985). *Phys. Rev. A*, **31**, 1695–1697.
Igarashi, T., Ihara, M., Kusunoki, T., Ohno, K., Isobe, T. & Senna, M. (2000). *Appl. Phys. Lett.* **76**, 1549.
Jeong, I.-K., Heffner, R. H., Graf, M. J. & Billinge, S. J. L. (2003). *Phys. Rev. B*, **67**, 104301.
Kalinko, A., Evarestov, R. A., Kuzmin, A. & Purans, J. (2009). *J. Phys. Conf. Ser.* **190**, 012080.
Kalinko, A. & Kuzmin, A. (2013). *J. Phys. Conf. Ser.* **430**, 012075.
Klueh, R., Maziasz, P., Kim, I., Heatherly, L., Hoelzer, D., Hashimoto, N., Kenik, E. & Miyahara, K. (2002). *J. Nucl. Mater.* **307–311**, 773.
Kuzmin, A. (1995). *Physica B*, **208–209**, 175–176.
Kuzmin, A., Efimov, V., Efimova, E., Sikolenko, V., Pascarelli, S. & Troyanchuk, I. (2011). *Solid State Ion.* **188**, 21–24.
Kuzmin, A. & Evarestov, R. A. (2009). *J. Phys. Condens. Matter*, **21**, 055401.
Lau, K. C. & Dunlap, B. I. (2011). *J. Phys. Condens. Matter*, **23**, 035401.
Lee, P. A., Citrin, P. H., Eisenberger, P. & Kincaid, B. M. (1981). *Rev. Mod. Phys.* **53**, 769–806.
Lindau, R., Möslang, A., Schirra, M., Schlossmacher, P. & Klimenkov, M. (2002). *J. Nucl. Mater.* **307–311**, 769–772.
Liu, S., Odette, G. & Segre, C. (2014). *J. Nucl. Mater.* **445**, 50–56.
Lu, J., Lu, J., Murai, T., Takaichi, K., Uematsu, T., Ueda, K., Yagi, H., Yanagitani, T. & Kaminskii, A. A. (2001). *Jpn. J. Appl. Phys.* **40**, L1277–L1279.
McGreevy, R. L. & Pusztai, L. (1988). *Mol. Simul.* **1**, 359–367.
Menut, D., Béchade, J., Cammelli, S., Schlutig, S., Sitaud, B. & Solari, P. L. (2015). *J. Mater. Res.* **30**, 1392–1402.
Muñoz, M., Argoul, P. & Farges, F. (2003). *Am. Mineral.* **88**, 694–700.
Palko, J. W., Kriven, W. M., Sinogeikin, S. V., Bass, J. D. & Sayir, A. (2001). *J. Appl. Phys.* **89**, 7791.
Pouchon, M., Kropf, A., Froideval, A., Degueldre, C. & Hoffelner, W. (2007). *J. Nucl. Mater.* **362**, 253–258.
Rehr, J. J. & Albers, R. C. (2000). *Rev. Mod. Phys.* **72**, 621–654.
Repelin, Y., Proust, C., Husson, E. & Beny, J. M. (1995). *J. Solid State Chem.* **118**, 163–169.
Sapelkin, A. V. & Bayliss, S. C. (2002). *Phys. Rev. B*, **65**, 172104.

Schmechel, R., Kennedy, M., von Seggern, H., Winkler, H., Kolbe, M., Fischer, R. A., Xaomao, L., Benker, A., Winterer, M. & Hahn, H. (2001). *J. Appl. Phys.* **89**, 1679.
Schneibel, J., Liu, C., Hoelzer, D., Mills, M., Sarosi, P., Hayashi, T., Wendt, U. & Heyse, H. (2007). *Scr. Mater.* **57**, 1040–1043.
Sevillano, E., Meuth, H. & Rehr, J. J. (1979). *Phys. Rev. B*, **20**, 4908–4911.
Sun, J., Qiu, X.-P., Wu, F. & Zhu, W.-T. (2005). *Int. J. Hydrogen Energy*, **30**, 437–445.
Swamy, V., Dubrovinskaya, N. A. & Dubrovinsky, L. S. (1999). *J. Mater. Res.* **14**, 456–459.
Timoshenko, J., Anspoks, A., Kalinko, A. & Kuzmin, A. (2014*b*). *Phys. Status Solidi (C)*, **11**, 1493.
Timoshenko, J., Anspoks, A., Kalinko, A. & Kuzmin, A. (2014*c*). *Acta Mater.* **79**, 194–202.
Timoshenko, J., Anspoks, A., Kalinko, A. & Kuzmin, A. (2014*d*). *Phys. Scr.* **89**, 044006.
Timoshenko, J., Anspoks, A., Kalinko, A. & Kuzmin, A. (2015). *Phys. Status Solidi A*, **212**, 265–273.
Timoshenko, J. & Kuzmin, A. (2009). *Comput. Phys. Commun.* **180**, 920–925.
Timoshenko, J., Kuzmin, A. & Purans, J. (2011). *Centr. Eur. J. Phys.* **9**, 710.
Timoshenko, J., Kuzmin, A. & Purans, J. (2012). *Comput. Phys. Commun.* **183**, 1237–1245.
Timoshenko, J., Kuzmin, A. & Purans, J. (2013). *J. Phys. Conf. Ser.* **430**, 012012.
Timoshenko, J., Kuzmin, A. & Purans, J. (2014*a*). *J. Phys. Condens. Matter*, **26**, 055401.
Ubaldini, A. & Carnasciali, M. M. (2008). *J. Alloys Compd.* **454**, 374–378.
Ukai, S. & Fujiwara, M. (2002). *J. Nucl. Mater.* **307–311**, 749.
Wang, S., Zhang, J., Luo, D., Gu, F., Tang, D., Dong, Z., Tan, G., Que, W., Zhang, T., Li, S. & Kong, L. (2013). *Prog. Solid State Chem.* **41**, 20–54.
Xu, Y.-N., Gu, Z.-Q. & Ching, W. Y. (1997). *Phys. Rev. B*, **56**, 14993–15000.
Yano, J. & Yachandra, V. (2009). *Photosynth. Res.* **102**, 241–254.
Yashiro, K., Yamaguchi, A., Tanaka, M., Okuda, T., Koga, K. & Segi, T. (2012). *Mater. Trans.* **53**, 401–406.